International Journal of Mass Spectrometry 468 (2021) 116640

Contents lists available at ScienceDirect

International Journal of Mass Spectrometry

journal homepage: www.elsevier.com/locate/ijms

Full Length Article

ESI-IM-MS reveals the metal binding of three analog methanobactin peptides with different numbers of free Cys at physiological pH

Rajpal Vangala, Laurence A. Angel*

Department of Chemistry, Texas A&M University-Commerce, 2600 S Neal Street, Commerce, TX, 75428, USA

ARTICLE INFO

Article history:
Received 15 February 2021
Received in revised form
25 May 2021
Accepted 28 May 2021
Available online 1 June 2021

Keywords:
Metal-peptide complexes
Cysteine metal binding
Histidine metal binding
2His-2Cys motif
Alternative metal binding peptides

ABSTRACT

Three analog methanobactin (amb_7) peptides containing the primary structure acetyl-Leu_1-His_2-Cys_3-Gly_4-Ser_5-Cys_6-Tyr_7-Pro_8-His_9-Cys_{10}-Ser_{11}-Cys_{12}-Met_{13} but differing by the number of disulfide bridges, have been studied for their reactivity with Fe(III), Mn(II), Co(II), Ni(II), Cu(II), Zn(II), Ag(I), and Pb(II) using electrospray ionization-ion mobility-mass spectrometry (ESI-IM-MS) and fluorescence quenching. The Pb(II) bound only with the $amb_{7\text{-}0}$ (0 disulfide bonds), Zn(II) only to $amb_{7\text{-}0}$ and $amb_{7\text{-}1}$ (1 disulfide bond), Ni(II) only to $amb_{7\text{-}1}$ and $amb_{7\text{-}2}$ (2 disulfide bonds), and Cu(II) to $amb_{7\text{-}2}$, concomitant with the oxidation of $amb_{7\text{-}0}$ and $amb_{7\text{-}1}$. The reduction of Cu(II) to Cu(I) resulted with 1-4Cu(I) binding to $amb_{7\text{-}1}$ and $amb_{7\text{-}0}$, while Ag(I) also exhibited 1-6 Ag(I) ions binding through a mechanism indicative of labile proton exchange. The binding of the oxidized Co(III/V) and Mn(III/V) were observed at pH 9 and 11, while Fe(III) did not exhibit significant binding. The observed negatively charged complexes were consistent with the deprotonation of the metal sites of Cys, His, carboxyl terminus and indicative of ion-ion interactions with the metal at pH 7, 9, and 11. The positively charged complexes were indicative of ion-dipole metal binding but at pH 9 and pH 11 gave results similar to those of the negative ion analyses. Fluorescence quenching also qualitatively agreed with the ESI-IM-MS results providing evidence that they revealed the solution-phase metal binding behavior of amb_7.

1. Introduction

Methanotrophs are differentiated from other microorganisms in the characteristic feature of using methane as their only source of carbon and energy. Methanotrophs synthesize the methanobactin peptide [1–3] which plays an important role in acquiring copper, a metal which is a cofactor of the enzyme methane monooxygenase, which catalyzes the oxidation of methane to methanol the precursor of formaldehyde which is used to synthesize various essential metabolites [4]. Methanobactins have the potential as therapeutics in reducing copper toxicity as in Indian childhood cirrhosis, Wilson's disease, and Menkes disease [5–8].

The methanobactin from *Methylosinus trichosporium* OB3b is the most studied methanobactin (mb-OB3b) and has the structure *1-(N-[mercapto-(5-oxo-2-(3-methylbutanoyl)-oxazol-(Z)-4-ylidene) methyl]-Gly_1-Ser_2-Cys_3-Tyr_4)-pyrrolidin-2-yl-(mercapto-[5-oxo-oxazol-(Z)-4-ylidene]methyl)-Ser_5-Cys_6-Met_7* (Fig. 1). [9–18] In mb-OB3b's native form, amino acids and enethiol oxazolone functional groups are present in its sequence and a disulfide bridge is formed between the Cys_3 and Cys_6 residues [18]. Copper-bound methanobactin has a pyramid-like shape with the copper ion attached at the base of the pyramid [19].

It has been postulated that mb-OB3b synthesis is driven by the modification of the ribosomal synthesized peptide **LCGSCYPCSCM** from the *M. trichosporium* OB3b genome by a series of deamination and cyclization steps to form the final compound [20]. The current study is with an alternative methanobactin peptide (amb_7) **acLHCGSCYPHCSCM** (Fig. 1) that has the similar amino acid sequence as mb-OB3b, but has the two post translational modified regions of the two enethiol oxazolone groups replaced with two His-Cys groups. The primary structure of amb_7 includes four Cys and our study shows how the formation of disulfide bridges between the Cys affect the amb_7 metal binding. The new investigation includes the comparative metal binding of Fe(III), Mn(II), Co(II), Ni(II), Cu(II), Zn(II), Ag(I), and Pb(II) by $amb_{7\text{-}0}$ (zero disulfide bridges), $amb_{7\text{-}1}$ (one disulfide bridge) and $amb_{7\text{-}2}$ (two disulfide bridges) using the positive and negative ion ESI-IM-MS analyses of aqueous solutions prepared at pH 5, 7, 9, and 11. The results indicate

* Corresponding author. Department of Chemistry, Texas A&M University-Commerce, 2600 S Neal St., Commerce, TX, 75428, USA.
E-mail address: Laurence.Angel@tamuc.edu (L.A. Angel).

https://doi.org/10.1016/j.ijms.2021.116640
1387-3806/

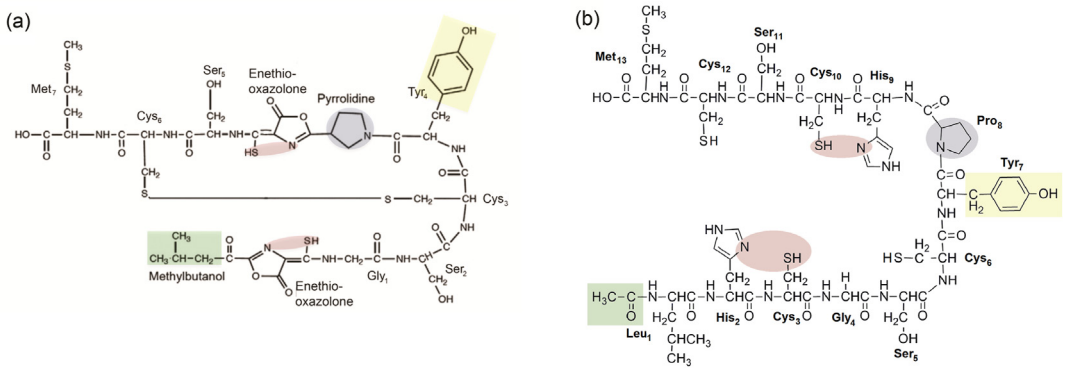

Fig. 1. The primary structure of **a)** methanobactin from *Methylosinus trichosporium* OB3b showing *N*-terminal blocking methyl butanol (green), the pyrrolidine ring (blue), the 2N2S enethiol-oxazolone binding sites (brown), and the Tyr (yellow) and **b)** alternative methanobactin $amb_{7\text{-}0}$ showing *N*-terminal blocking acetyl (green), the proline ring (blue), the 2His-2Cys binding sites (brown), and Tyr (yellow).

that the negative ion analyses predominantly measures the interactions with the metal binding via the Cys thiolates, His imidazoles or imidazolates, and the carboxylate terminus, while the positive ion analyses measures ion-dipole binding through the carbonyl oxygens or His imidazoles. These binding behaviors have been indicated before and the results presented here are compared to our previously published analyses of the metal binding selectivity of mb-OB3b [21, 22] and amb_1 to amb_5 [23–31].

2. Experimental section

2.1. Chemical reagents and metal ions

Two amb_7 samples were synthesized (neobiolab.com) the first was designated $amb_{7\text{-}2}$ (98% purity) which contained 2 disulfide bonds between the 4Cys. The second sample $amb_{7\text{-}0\text{-}1}$ contained 32% $amb_{7\text{-}0}$, (0 disulfide bonds) and 65% $amb_{7\text{-}1}$ (1 disulfide bond). The $MnCl_2$, $CoCl_2$, $NiCl_2$, $CuCl_2$, $Cu(NO_3)_2$ (99.99% or higher trace metal grade), and poly-DL-alanine were purchased from Sigma-Aldrich (www.sigmaaldrich.com). $FeCl_3$, $AgNO_3$ and $ZnCl_2$ (ACS grade 98%+) were purchased from Alfa Aesar (www.alfa.com/en). $PbCl_2$ (ACS grade) was purchased from Mallinckrodt (currently Avantor) (www.avantormaterials.com). Solutions were prepared using deionized (DI) water (>18.2 MΩ cm, MilliQ, Millipore). NH_4OH (trace metal grade) and CH_3COOH (Optima grade) were purchased from Fisher Scientific (http://www.Fishersci.com).

2.2. Stock solution preparation

The $amb_{7\text{-}0\text{-}1}$ or $amb_{7\text{-}2}$ samples were prepared at 12.5 mM in DI H_2O in 50 μL portions and frozen at −80 °C until use. Metal ion stock solutions were prepared at 125 mM and acetic acid and ammonium hydroxide solutions were prepared at 1.0 M and diluted further as needed for each experiment.

2.3. Metal binding and collision-induced dissociation experiments

The metal binding experiments were analyzed by mixing 1:1.5 molar equivalents of amb_7:metal ion (amb_7 8.75 μM) in dilute acetic acid or ammonium hydroxide aqueous solutions prepared for the desired pH of the sample. Each sample was incubated at room temperature for 1 h before analyses and the final pH measured by a calibrated Orion 98 micro pH electrode.

2.4. Waters Synapt High-Definition Mass Spectrometer (HDMS)

The samples were analyzed using the Waters Synapt High-Definition Mass Spectrometer (G1) equipped with an electrospray ionization (ESI) source in a quadrupole-ion mobility-orthogonal time-of-flight configuration [32]. Before sample injection, the inlet line was flushed with 10% NH_4OH (in H_2O, v/v) and 10% acetic acid (in H_2O, v/v) to remove any trace metal ion and counter-ion contaminates. Samples were directly injected via a syringe pump into the ESI source with gentle ionization and transmission conditions to maintain the populations and structures of the amb_7 from the solution phase. Details of the tuning conditions are in the supporting information.

2.5. Data analysis of metal ion binding

The ESI-IM-MS analyses identified the arrival time and *m/z* for each amb_7 species, including any coincidental *m/z* species. Each species, identified based on their *m/z* isotope patterns, had their arrival time distributions (ATD) separated and extracted using Driftscope 2.1. The MassLynx 4.1 software determined the centroid of each ATD, for calculating the average collision cross sections, and the area under the ATD curve to measure the proportions of the various amb_7 species. The summation of the integrated ATD for all extracted species from each sample converted to the relative percent intensity scale.

2.6. Collision-induced dissociation

To study the CID of the amb_7 complexes, the isotope distribution of the precursor complex ion were resolved by the linear quadrupole, and either dissociated in the trap T-wave cell or passed through the trap and the IM cells, and dissociated in the transfer T-wave cell using the lab-frame collision energy (CE) controlled by the entrance lens [33]. The precursor and product ions were *m/z* analyzed by the TOF and identified by matching their isotope patterns to their theoretical isotope patterns from the MassLynx 4.1 software. The nomenclature and identity of the amb_7 fragmentation are in the supporting information.

2.7. Collision cross-sections

A calibration method determined the collision cross sections (CCS) of the amb_7 complexes using published CCS measured in helium for poly-DL-alanine ions measured in a radio-frequency confining drift cell [34–36]. The trap T-wave was operated with 6.0 V entrance

voltage and a pressure of 2.25×10^{-2} mbar with an argon gas flow of 3.0 mL/min. The trap served as a storage cell for gating ions into the ion mobility (IM) T-wave ion guide using a trap DC bias of 12.0 V. The IM ion guide was operated at a pressure of 0.516 mbar with a flow rate of 20.0 mL min^{-1} N_2 buffer gas with ramped T-wave heights of 18.3–24.0 V and ramped T-wave velocities of 900–1500 m s^{-1} (+) or T-wave heights of 7.0–25.0 V and 200–500 m s^{-1} (−) for every sweep of the IM T-wave ion guide. Further details of the calibration procedure are in the supporting information.

2.8. Fluorescence quenching

The fluorescence quenching analyses were based on the relationship between the fluorescence intensity during the titration of $amb_{7\text{-}0\text{-}1}$ with the static quenching metal ion [37]. Briefly, Tyr_7 of amb_7 was the fluorophore with $\lambda_{ex} = 284$ nm and $\lambda_{em} = 316$ nm, and the intensity of fluorescence was measured during the titration of amb_7 with the metal ion quencher. The binding constant *K* was determined using the relationship between the fluorescence intensity and the concentration of unbound amb_7 [37]. Further details are in the supporting information.

2.9. Computational methods

The semi-empirical method PM6, [38] with its capability for modeling biomolecules and transition metals, was used to locate geometry optimized, gas-phase conformations of the amb_7 complexes using Gaussian 09 [39]. Parametrization methods have previously been used in the chemical dynamics studies of the dissociation of the amb_5-Zn(II) complex [40,41] and the accuracy of these methods to describe molecules containing Zn(II) has been reported by Truhlar et al. [42] To locate the lowest energy conformers, the starting structures for the geometry optimizations tested various protonation states of the carboxyl terminus, His, Cys, and Tyr substituent sites and the backbone amide nitrogens, which combined with the metal ion gave the overall charge of the complex. The CCS of these conformers were calculated using the ion size scaled Lennard-Jones (L-J) method developed by the Bowers group from the Department of Chemistry and Biochemistry at the University of California - Santa Barbara [43]. The L-J method calculates the CCS of the complex by projecting it onto a randomly selected plane in space, and an L-J collision circle is drawn at the position of each projected atom. Using a square of an area that encloses the projected molecule, randomly chosen points are counted as a collision if they are inside these L-J circles. The ratio of collisions to the number of chosen points multiplied by the area enclosing the complex is the CCS of that particular projection. The process is repeated for many different randomly selected projections until a convergence of the CCS is found. Ten separate measurements were made of each conformer to determine the final mean and standard deviation. The L-J method does not provide absolute CCS for this size of the amb_7 peptide (it is recommended for peptides with 20–150 atoms). Therefore, to compare the L-J CCS with the ESI-IM-MS measured CCS we used an additional scaling factor of 0.90 which allowed direct comparison of the relative sizes of the complexes that differ by their number of protons, the metal ion, and number of disulfide bonds.

3. Results

3.1. Identification of the position of the disulfide bonds of $amb_{7\text{-}1}$ and $amb_{7\text{-}2}$

The CID of the positively charged $amb_{7\text{-}0}$, with zero disulfide bonds, produced a series of b and y ions readily identified based on the fragmentation of the backbone as shown in Fig. 2a. From the CID of $amb_{7\text{-}1}$ containing one disulfide bond (Fig. 2b) the position of the disulfide bond was identified from the b_6-2 and b_7-2 fragments that differ by the mass of two hydrogen atoms from b_6 and b_7 of $amb_{7\text{-}0}$. These fragments show a disulfide bond existed between Cys_3-Cys_6 in $amb_{7\text{-}1}$. The appearance of y_7-2 ion in Fig. 2b also indicated some of the $amb_{7\text{-}1}$ had the disulfide bond between Cys_{10}-Cys_{12}. The CID of $amb_{7\text{-}1}$ still produced a wide coverage of b and y backbone cleavages indicating that there were not significant populations of $amb_{7\text{-}1}$ with disulfide bonds from the *C*-terminal side to the *N*-terminal sides *i.e.*, Cys_3-Cys_{12} or Cys_3-Cys_{10} that would restrict the formation of these product ions. For $amb_{7\text{-}2}$ containing two disulfide bonds (Fig. 2c) the inclusion of the y_5-2 and y_6-2 ions as well as the y_7-2, b_6-2 and b_7-2 ions also showed that the two disulfide bonds predominantly existed between the Cys_3-Cys_6 and the Cys_{10}-Cys_{12}. Large fragments such as y_{11}-4 that include all 4Cys were also consistent with these two disulfide bonds.

3.2. Negatively charged amb_7 complexes

The incubation of amb_7 peptides with the selected metal ions resulted in metal-amb_7 complexes and metal-free amb_7, apart from with Fe(III) which did not form negatively charged complexes. Fig. 3 shows the percent formation of the metal complexes from each metal from prepared solutions at pH 5, 7, 9, and 11. At pH 5 the incubation of $amb_{7\text{-}0\text{-}1}$ with the metal ion resulted with the metal-free amb_7 remaining as $amb_{7\text{-}0}$ or $amb_{7\text{-}1}$, apart from the solution containing Cu(II) which had oxidized the $amb_{7\text{-}0}$ and $amb_{7\text{-}1}$ to $amb_{7\text{-}2}$. At pH 7, 9, and 11 the oxidation of the metal-free $amb_{7\text{-}0}$ and $amb_{7\text{-}1}$ to $amb_{7\text{-}2}$ was the case for all the amb_7:metal samples showing the 1-h incubation with pH $\geq$ 7 increased the oxidation of the thiol groups. The incubation of $amb_{7\text{-}2}$ with the metal ions did not change the oxidation state of $amb_{7\text{-}2}$.

Fig. 3 shows at pH 5 the negative ion analyses displayed the formation of $amb_{7\text{-}0}$ complexes with Zn(II) and Pb(II) and $amb_{7\text{-}2}$ complexes with Co(II), Cu(II) and Ag(I). At pH 7 there was a significant increase in the formation of $amb_{7\text{-}0}$ complexes with Pb(II) and 2Zn(II), as well as new $amb_{7\text{-}1}$ complexes with Zn(II), 1-2Ni(II) and Co(III), and oxidized $amb_{7\text{-}2}$ complexes with Cu(II). There was a further increase in the formation of the $amb_{7\text{-}0}$ complexes of Pb(II), $amb_{7\text{-}1}$ complexes of Zn(II), 1-2Ni(II) and $amb_{7\text{-}2}$ complexes of 1-2Cu(II) at pH 9, with additional complexes for $amb_{7\text{-}0}$ of Mn(III/V) or 2-4Ag(I) and $amb_{7\text{-}1}$ with Ag(I). At pH 11, the binding pattern was similar to pH 9, but with a significant increase in Ag(I) and Co(III/V) binding and a decrease in Zn(II) binding, which may be competition from Zn(II) hydroxide formation.

3.3. Positively charged amb_7 complexes

Fig. 4 shows the percent formation of the metal complexes at each pH from the positive ion analyses. At pH 5 each of the metal ions were associated with one of the amb_7 species, even Fe(III) formed 10% of the $[amb_{7\text{-}2}+Fe(II)]^{2+}$ complex at pH 5 (data not shown) but did not form complexes at pH 7, 9, or 11. In general the metal binding at pH 5 seemed to exhibit non-specific binding which was independent of the metal, because the metal ions of Mn(II), Co(II), Ni(II) and Zn(II) exhibited comparable percent binding to $amb_{7\text{-}1}$ and $amb_{7\text{-}2}$ and Cu(II) also exhibited comparable binding with $amb_{7\text{-}2}$. The redox activity of Cu(I/II) produced complexes of 4Cu(I) with $amb_{7\text{-}0}$ and 2-3Cu(I) with $amb_{7\text{-}1}$, which suggested an exchange mechanism for the labile protons of Cys or His resulting in linear bridged Cu(I) binding [27,28,30]. The Pb(II) formed complexes with $amb_{7\text{-}0}$ and $amb_{7\text{-}2}$ and Ag(I) formed complexes of 2-6 Ag(I) with $amb_{7\text{-}0}$ and 1-2Ag(I) with $amb_{7\text{-}1}$ or $amb_{7\text{-}2}$.

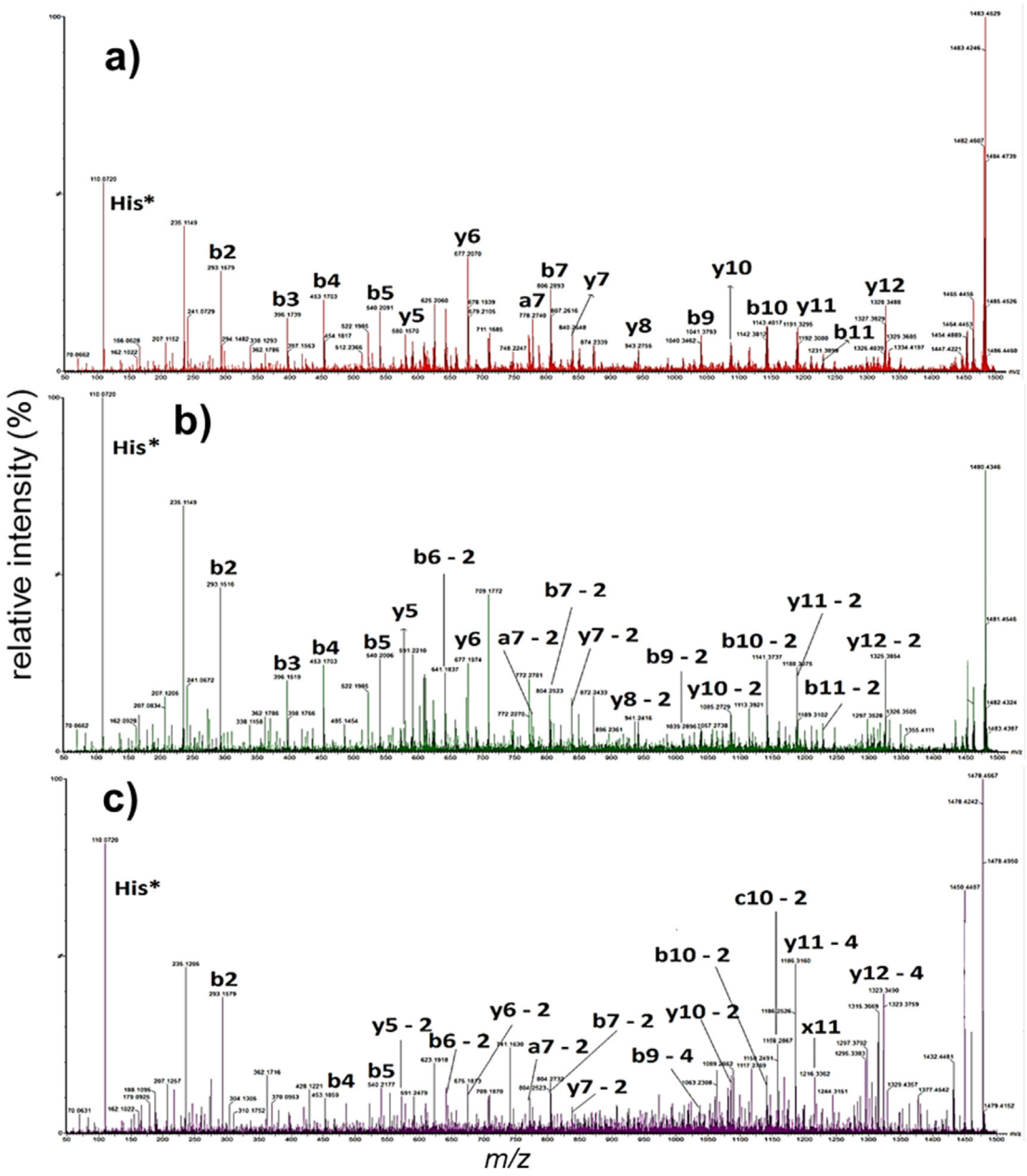

Fig. 2. The products of the collision-induced dissociation of **a)** $amb_{7\text{-}0}$ **b)** $amb_{7\text{-}1}$ and **c)** $amb_{7\text{-}2}$ using transfer collision energy 60 V, 60 V, and 65 V, respectively.

At pH 7 Mn(II), Co(II), and Zn(II) again produced very similar reactivity's for binding to $amb_{7\text{-}1}$ and $amb_{7\text{-}2}$ and Ni(II) also showed similar binding to $amb_{7\text{-}1}$. The Pb(II) bound only to $amb_{7\text{-}0}$ and Cu(I/II) bound with $amb_{7\text{-}1}$ and $amb_{7\text{-}2}$ but lower than at pH 5. At pH 9 and 11, the differences between the metal bindings became more distinctive. Nickel (II) and Zn(II) were only chelated by $amb_{7\text{-}1}$, Cu(II) was only chelated by $amb_{7\text{-}2}$, and 2-6Ag(I) were chelated by $amb_{7\text{-}0}$ or 1-2Ag(I) were chelated by $amb_{7\text{-}1}$. The six Ag(I) ions corresponded to the six total sites of the 4Cys and 2His, which indicated that Ag(I) acts through proton exchange replacing the labile protons on either His or Cys. The Pb(II) was only chelated by $amb_{7\text{-}0}$, and Co(III/V) and Mn(III/V) were also observed to bind to $amb_{7\text{-}1}$ and $amb_{7\text{-}0}$, respectively.

3.4. Fluorescence quenching of amb_7 by the selected metal ions

To evaluate whether the metal binding behavior of amb_7 with the metal ions observed by ESI-IM-MS was symptomatic of the solution-phase chemistry, a fluorescence quenching study of the $amb_{7\text{-}0\text{-}1}$ with addition of the selected metal as a quencher was conducted at pH 9. The fluorophore is Tyr_7 and the π-metal cation interaction is the proposed mechanism for fluorescence quenching [44]. The fluorescence quenching by the metal ion addition (Fig. 5) suggests that Ni(II), Cu(II), Ag(I), and Pb(II) exhibited a higher reactivity with $amb_{7\text{-}0\text{-}1}$ than Mn(II), Co(II), and Fe(III). This correlates with the ESI-IM-MS results at pH 9 (Figs. 3 and 4), especially that of the positive ion analyses, that showed Ni(II), Cu(II), Ag(I),

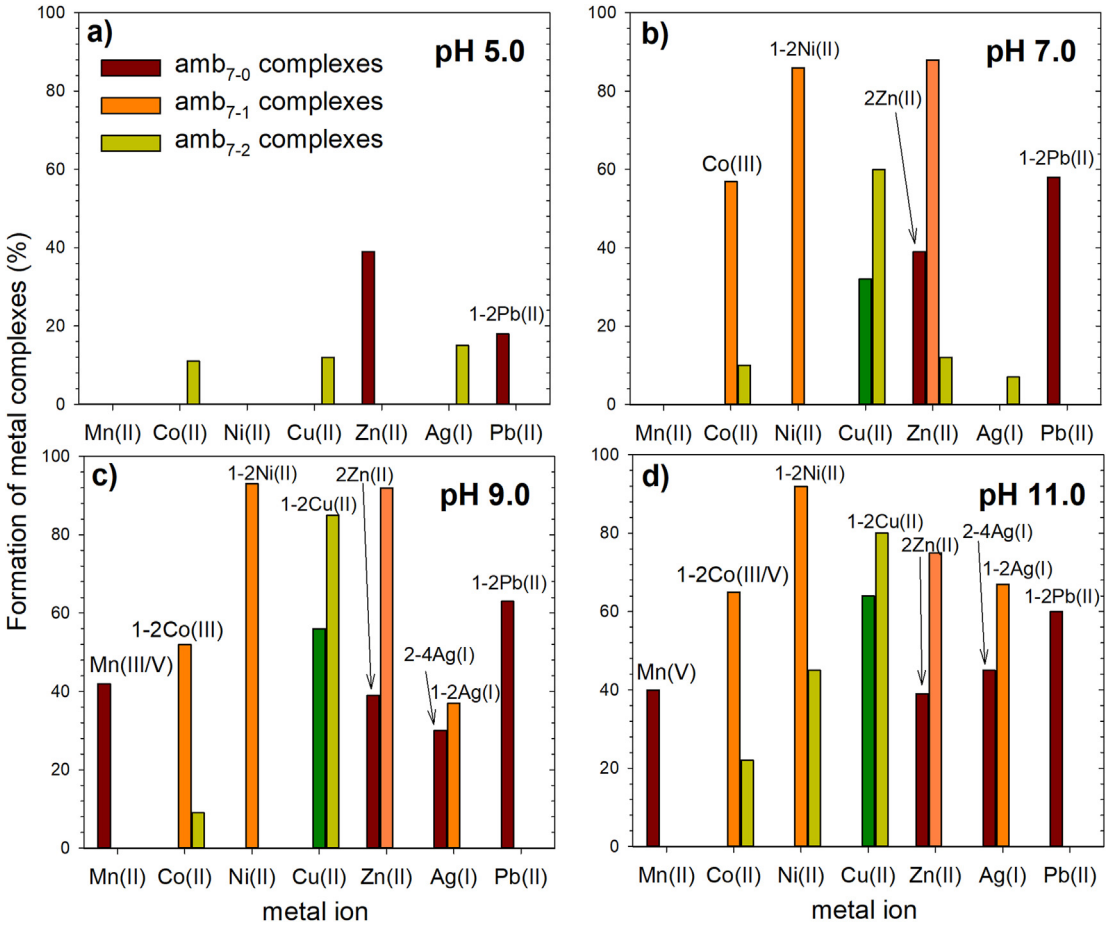

Fig. 3. The relative percent formation of $amb_{7\text{-}0}$ (brown) and $amb_{7\text{-}1}$ (orange) metal complexes from the $amb_{7\text{-}0\text{-}1}$+metal samples and the formation of $amb_{7\text{-}2}$ metal complexes (light green) from the $amb_{7\text{-}2}$:metal samples from the negative ion analyses of solutions prepared at pH 5, 7, 9, and 11. The formation of Cu(II) $amb_{7\text{-}2}$ complexes from the $amb_{7\text{-}0\text{-}1}$:metal sample is shown in dark green. Labels indicate whether there is multiple binding or change in the metal oxidation states.

and Pb(II) exhibited significantly more binding to $amb_{7\text{-}0\text{-}1}$ than Co(III), Mn(V) or Fe(III). The fluorescence results of Zn(II) were not included in Fig. 5 because the addition of Zn(II) resulted in a metal cation-enhanced fluorescence [44].

From the fluorescence quenching data the binding constants for the selected metal ions and amb_7 were estimated using a fluorescence quenching model that was previously applied to mb-OB3b [21], binding of TiO_2 to DNA [37] and flavonoids to bovine serum albumin [45]. The Cu(II) and Ag(I) exhibited the steepest initial increases in fluorescence quenching (Fig. 6) resulting in the highest binding constants $K = 5.07 \times 10^7$ and 1.36×10^5, respectively. The Cu(II) fluorescence quenching exhibited the least linear behavior and could only be fitted to the first 4 data points and was probably affected by the disulfide bond formation that accompanied the Cu(II) binding. For Cu(II) the average number of metal ions binding to amb_7 was $n = 1.76$, which was the highest for any of the metal ions studied (Fig. 6). For Ag(I) the number of metal ions binding was the second highest, $n = 1.23$, and indicative of the multiple Ag(I) binding. The formation constants of Ni(II) and Pb(II), $K = 1.88 \times 10^4$ and 1.97×10^4 with $n = 0.96$ and 0.98, respectively were the next highest. The Mn(II), Co(II), and Fe(III) showed the lowest binding constants of $K = 2.25 \times 10^3$, 42.6, and 7.67×10^3 (Fe(III) data not shown), respectively.

3.5. Collision cross sections of amb_7 complexes measured at pH 9

The comparison of the collision cross sections (CCS) of the amb_7 complexes are in Fig. 7. The negative ion species were $[amb_{7\text{-}0}-2H]^{2-}$, $[amb_{7\text{-}1}-2H]^{2-}$, $[amb_{7\text{-}2}-2H]^{2-}$, $[amb_{7\text{-}0}-7H+Mn(V)]^{2-}$, $[amb_{7\text{-}1}-5H+Co(III)]^{2-}$, $[amb_{7\text{-}1}-4H+Ni(II)]^{2-}$, $[amb_{7\text{-}2}-4H+Cu(II)]^{2-}$, $[amb_{7\text{-}1}-4H+Zn(II)]^{2-}$, $[amb_{7\text{-}1}-3H+Ag(I)]^{2-}$, and $[amb_{7\text{-}0}-4H+Pb(II)]^{2-}$. The $[amb_{7\text{-}0}-2H]^{2-}$ and $[amb_{7\text{-}1}-2H]^{2-}$ gave identical CCS, but the CCS of $[amb_{7\text{-}2}-2H]^{2-}$ was 5 Å^2 smaller presumably because it was more folded by the two disulfide bonds. All the negatively charged complexes exhibited CCS that were smaller than the free $amb_{7\text{-}0\text{-}1}$ and more similar to the CCS of $[amb_{7\text{-}2}-2H]^{2-}$ indicative that the negative ion complexes were also more folded due to their interactions with the metal ions. Nickel-bound $amb_{7\text{-}1}$ exhibited the smallest average CCS suggesting Ni(II) was the most tightly bound by $amb_{7\text{-}1}$ and consistent to the high formation of the Ni(II) complexes (Fig. 3).

The positive ion species $[amb_{7\text{-}0}+2H]^{2+}$, $[amb_{7\text{-}1}+2H]^{2+}$, $[amb_{7\text{-}2}+2H]^{2+}$, $[amb_{7\text{-}0}-H+Mn(III)]^{2+}$, $[amb_{7\text{-}1}-H+Co(III)]^{2+}$, $[amb_{7\text{-}1}+Ni(II)]^{2+}$, $[amb_{7\text{-}2}+Cu(II)]^{2+}$, $[amb_{7\text{-}1}+Zn(II)]^{2+}$, $[amb_{7\text{-}1}+H+Ag(I)]^{2+}$, and $[amb_{7\text{-}0}+Pb(II)]^{2+}$ are also compared in Fig. 7. The most striking observation is that their CCSs are 19–37 Å^2 larger than the CCS of $[amb_{7\text{-}2}+2H]^{2+}$, which was folded by the two

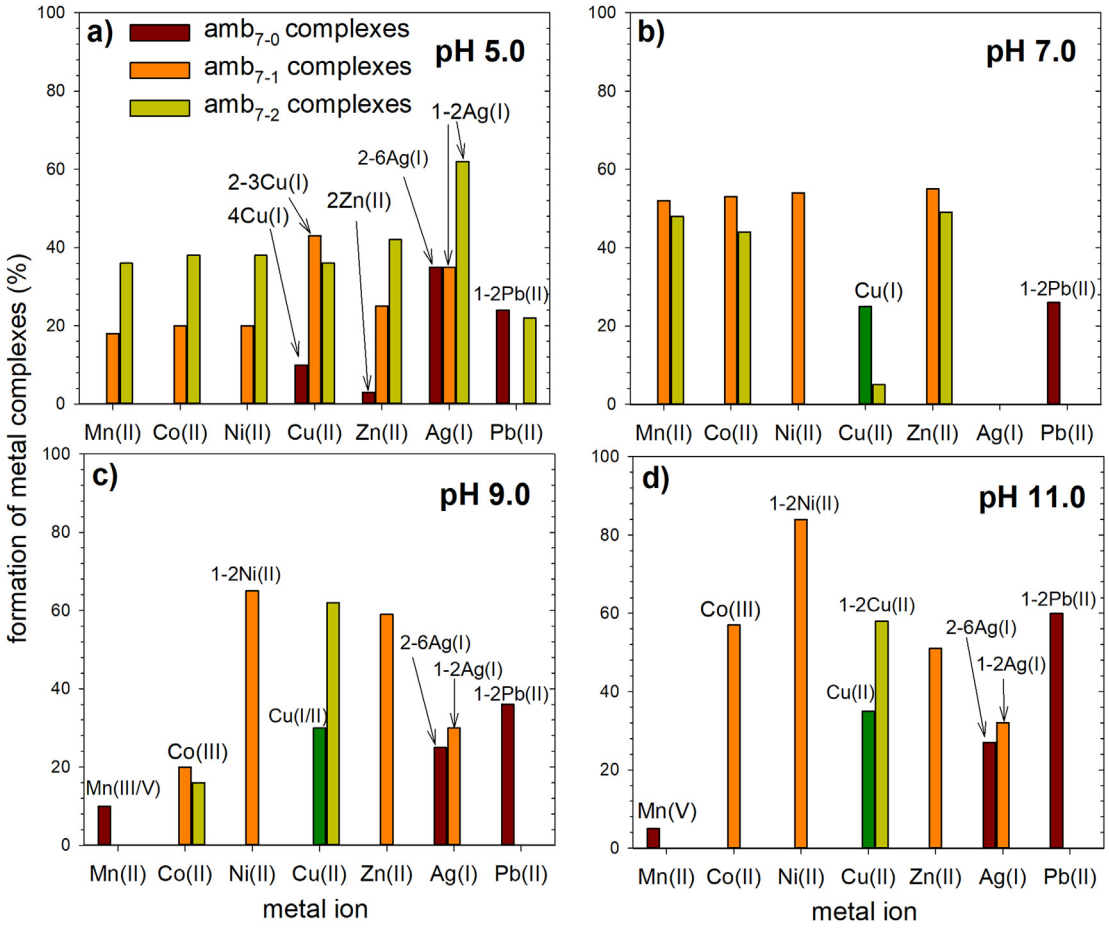

Fig. 4. The relative percent formation of $amb_{7\text{-}0}$ (brown) and $amb_{7\text{-}1}$ (orange) metal complexes from the $amb_{7\text{-}0\text{-}1}$+metal samples and the formation of $amb_{7\text{-}2}$ metal complexes (light green) from the $amb_{7\text{-}2}$:metal samples from the positive ion analyses of solutions prepared at pH 5, 7, 9, and 11. The formation of Cu(II) $amb_{7\text{-}2}$ complexes from the $amb_{7\text{-}0\text{-}1}$:metal sample is shown in dark green. Labels indicate whether there is multiple binding or change in oxidation states.

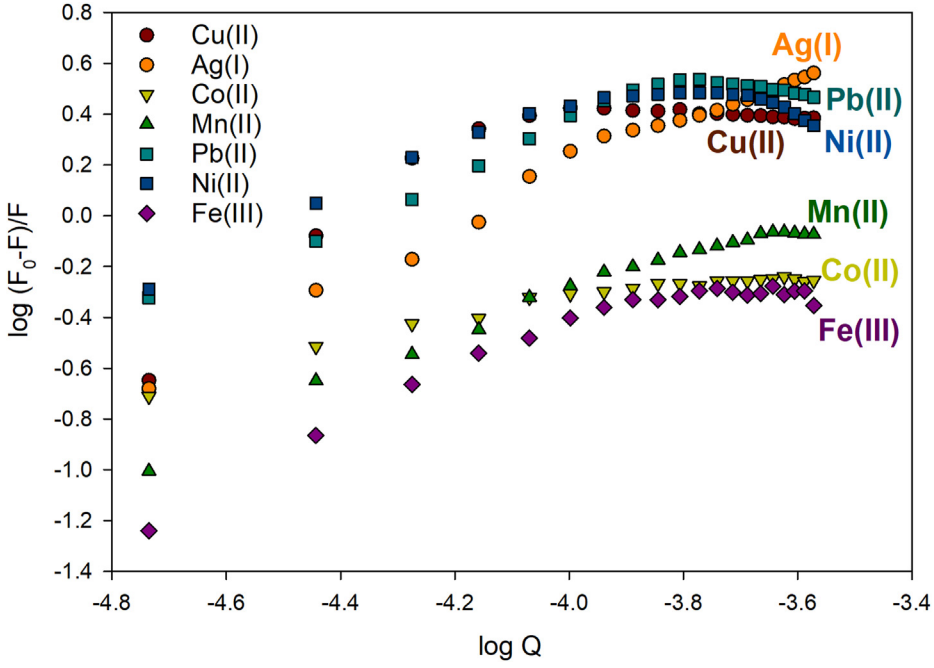

Fig. 5. The comparison of the fluorescence quenching by the titration of $amb_{7\text{-}0\text{-}1}$ with selected metal ions at pH 9.

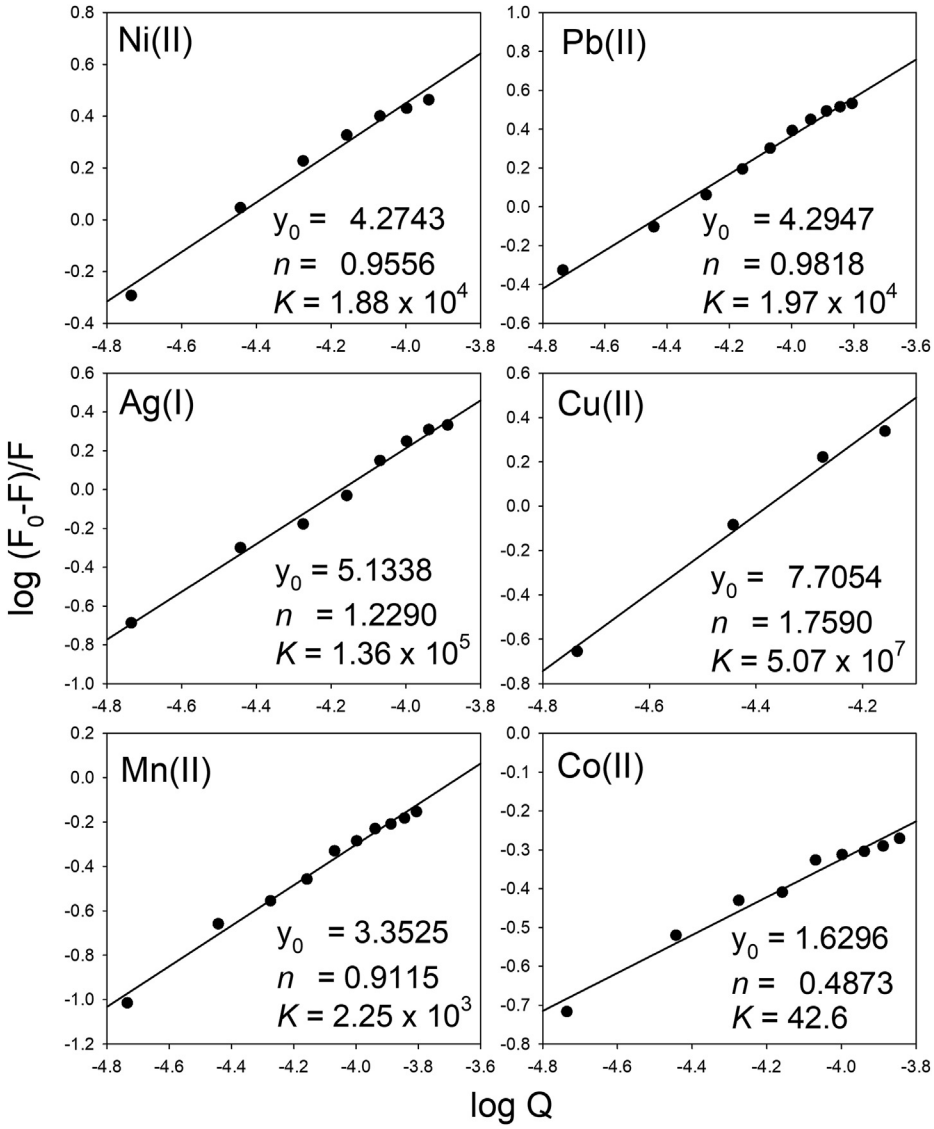

Fig. 6. Fluorescence quenching plots for the formation of the amb_7 complex with Ni(II), Pb(II), Ag(I), Cu(II), Mn(II) and Co(II) from solutions prepared at pH 9.

disulfide bonds and also significantly larger than their counterpart negative ions. These differences in CCS would correspond to the weaker ion-dipole interactions between the metal ion and the dipoles of His or carbonyl oxygens in the positive ion complexes compared to the ion-ion interactions between the metal ion and the thiolates, imidazolates and/or carboxylates in the negative ion complexes. The largest change in CCS was for the Pb(II)+amb_{7-0} complexes which shows that with no disulfide bonds the positive ion complex unfolds more than the complexes with disulfide bonds.

3.6. CID studies of metal complexes

The CID of negatively charged amb_7 and its metal complexes primarily produced the loss of H_2S and $2H_2S$ and information about their primary structure or metal binding sites was absent. However, the CID of the positively charged amb_7 gave nearly a complete set of b and y ions (Fig. 2) and the amb_7 metal complexes (Fig. 8) also gave sequence related a, b, c, and y type ions, giving information about their structure and how the metal ion binding affected their dissociation.

Fig. 8 and Table 1 shows the spectra and the identities of the product ions from the CID of the $[amb_{7-2}+Cu(II)]^{2+}$, $[amb_{7-0}-H+Mn(III)]^{2+}$, $[amb_{7-1}+Ni(II)]^{2+}$, and $[amb_{7-0}+Pb(II)]^{2+}$ complexes. The Cu(II) binding was observed with amb_{7-2}, where all the Cys were oxidized, which is indicative that Cu(II) coordinates with the imidazole rings of the 2His. The CID of the $[amb_{7-2}+Cu(II)]^{2+}$complex (Fig. 8a) is consistent with this because the main products were the b_9+Cu(II), b_{10}+Cu(II), and b_{11}+Cu(II) ions, which all included the potential His_2 and His_9 binding sites in their sequence. The formation of these b ions were through the loss of the *C*-terminus end of amb_{7-2}, which included the Cys_{10}-Cys_{12} disulfide bond and the formation of b_{10}+Cu(II) and b_{11}+Cu(II) must have been accompanied by the dissociation of this disulfide bond. This suggests the Cu(II) binding to His_2 and His_9 and the disulfide bond between Cys_3 and Cys_6, stabilized this section of amb_7 and made the Cys_{10}-Cys_{12} disulfide bond and backbone between b_9 to b_{11} labile by CID.

The CID of the $[amb_{7-0}-H+Mn(III)]^{2+}$ complex (Fig. 8b) gave the formation of c_{10}+Mn(III) and c_{11}+Mn(III) ions which again was loss of the *C*-terminus end of the amb_{7-0} but adjacent to the amide groups. There were no disulfide bonds but the labile *C*-terminal end

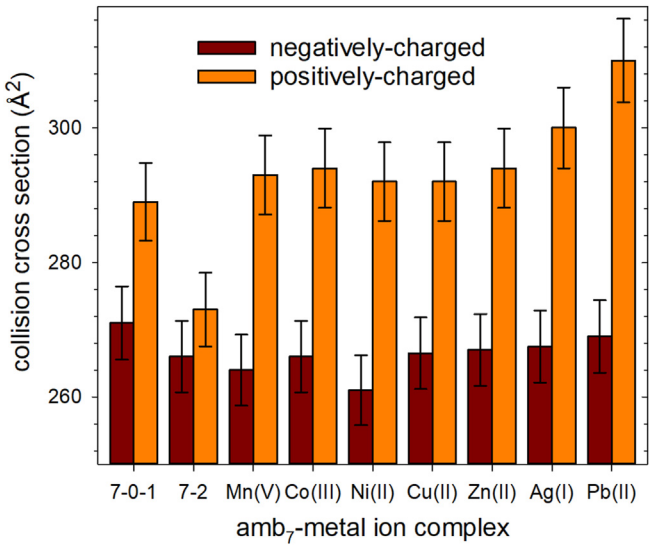

Fig. 7. The collision cross sections for $amb_{7\text{-}0\text{-}1}$, $amb_{7\text{-}2}$, and the selected metal bound amb_7 complexes from the negative and positive ion analyses measured from solutions at pH 9.

of amb_7 suggested that Mn(III) was also binding to His_2 and His_9. The CID of the $[amb_{7\text{-}1}+Ni(II)]^{2+}$ and $[amb_{7\text{-}0}+Pb(II)]^{2+}$ complexes produced the $y_{12}+Ni(II)/Pb(II)$ ion, which is the loss of the modified *N*-terminal end of amb_7 before His_2. The complexes also dissociated into the $a_9+Ni(II)/Pb(II)$ and $b_9+Ni(II)/Pb(II)$ product ions, which formed by loss of the *C*-terminus arm after His_9. These cleavages of amb_7 on either side of the His_2 and His_9 residues again indicate that these were the binding sites for Ni(II) and Pb(II), as they were for Cu(II) and Mn(III). The ion-dipole binding between the metal ion and the two imidazoles of His_2 and His_9 is consistent with the overall +2 charge of the complexes and that for positively charged complexes the free Cys and *C*-terminus remained protonated.

Table 1
The monoisotopic *m/z* and identity of product ions from the collision-induced dissociation of metal bound amb_7 complexes of Mn(III), Pb(II), Ni(II) and Cu(II).

Metal amb_7 complex	Mn(III)	Pb(II)	Ni(II)	Cu(II)
Precursor ion *m/z*	767.77	844.73	768.72	769.69
Identity of product ions and *m/z*				
−18 (H_2O)		835.73	759.73	
−36 ($2H_2O$)		826.72		
−66 (S_2H_2)	734.79			
y_{12} + Pb(II)/Ni(II)		767.19	691.18	
c_{11} + Mn(III)	649.73			
b_{11} + Cu(II)				645.68
c_{10} + Mn(III)	606.21			
b_{10} + Cu(II)/Pb(II)		675.19		602.16
b_9 + Pb(II)/Ni(II)/Cu(II)		623.68	547.66	550.66
a_9 + Pb(II)/Ni(II)		609.69	533.68	

However, for the negatively charged complexes the Cys were deprotonated as evidenced by the overall charge and the pH dependent metal binding behavior as the pH approaches the p*K*a of Cys. The availability of 2Cys, His and carboxylate terminus for binding the Ni(II) or Zn(II) in their negatively charged complexes has been well established by our studies of the smaller amb_1 and amb_5 peptides [24–26]. However, the thiolates in the negatively charged complexes are reduced to hydrogen sulfide during CID and the sequence information for determining their binding sites was absent.

3.7. Molecular modeling of amb_7 complexes

Guided by the experimental results, the geometry optimized conformers of selected complexes were located using PM6 and the results are shown in Fig. 9. The scaled L-J CCS of each conformer are also shown to compare the relative sizes of the complexes that differ by the number of protons, the metal ion, and number of disulfide bonds, giving a relative measure of the sizes the conformations.

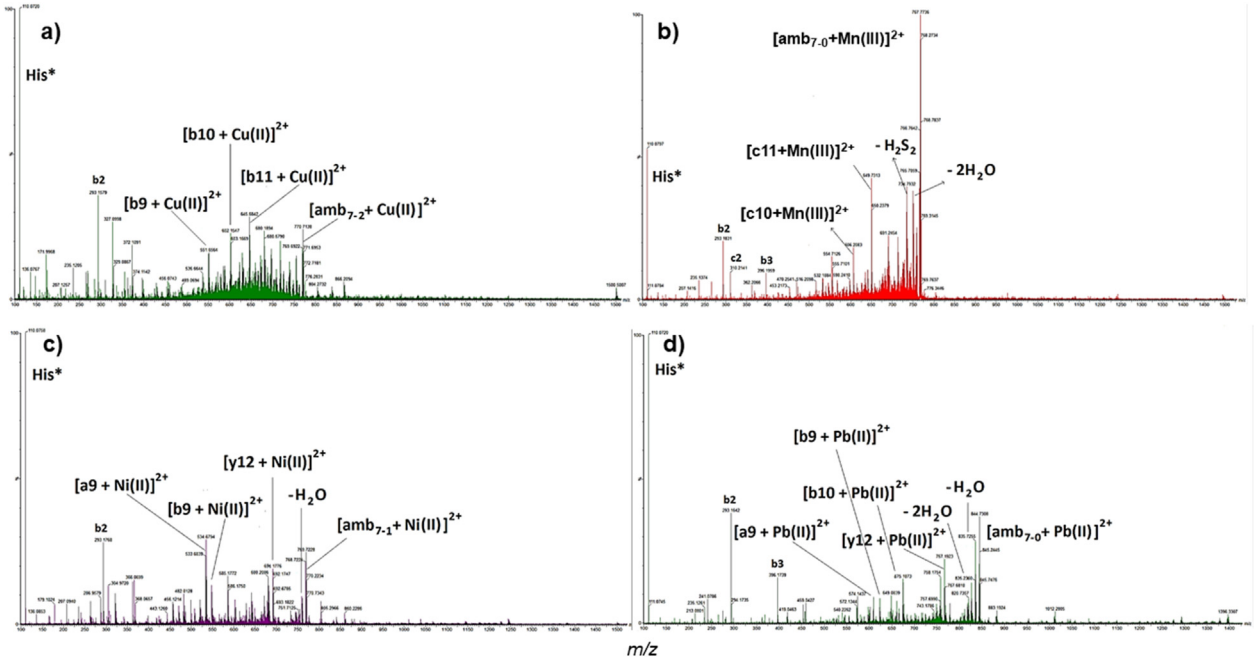

Fig. 8. The mass spectra of the collision induced dissociation of **a)** $[amb_{7\text{-}2}+Cu(II)]^{2+}$ with trap collision energy 35 V, **b)** $[amb_{7\text{-}0}-H+Mn(III)]^{2+}$ 30 V, **c)** $[amb_{7\text{-}1}+Ni(II)]^{2+}$ 35 V, and **d)** $[amb_{7\text{-}0}+Pb(II)]^{2+}$ 35 V.

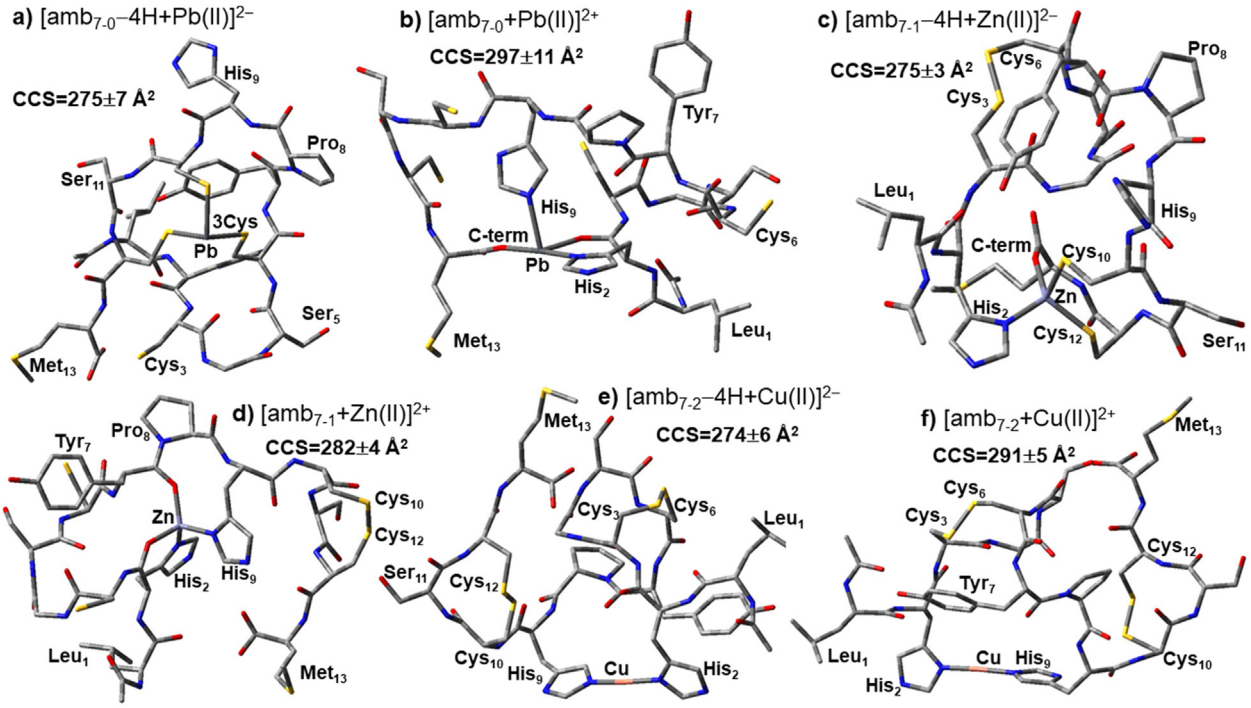

Fig. 9. PM6 geometry optimized conformers of amb_7 complexes **a)** $[amb_{7\text{-}0}-4H+Pb(II)]^{2-}$, **b)** $[amb_{7\text{-}0}+Pb(II)]^{2+}$, **c)** $[amb_{7\text{-}1}-4H+Zn(II)]^{2-}$, **d)** $[amb_{7\text{-}1}+Zn(II)]^{2+}$, **e)** $[amb_{7\text{-}2}-4H+Cu(II)]^{2-}$, and **f)** $[amb_{7\text{-}2}+Cu(II)]^{2+}$. The scaled Lennard-Jones collision cross sections (CCS) for each complex are shown.

The Pb(II) was only chelated by $amb_{7\text{-}0}$ and Fig. 9a and b compares the complexes of $[amb_{7\text{-}0}-4H+Pb(II)]^{2-}$ and $[amb_{7\text{-}0}+Pb(II)]^{2+}$. The Pb(II) is chelated by 3Cys thiolate groups in a trigonal pyrimadal geometry for $[amb_{7\text{-}0}-4H+Pb(II)]^{2-}$ with the unbound carboxylate terminus the other deprotonated site. The 2His imidizoles and two carbonyl oxygens from the backbone of His_2 and the protonated *C*-terminus are the four ion-dipole interactions for $[amb_{7\text{-}0}+Pb(II)]^{2+}$. The L-J CCS of the conformation of $[amb_{7\text{-}0}-4H+Pb(II)]^{2-}$ shows it is 22 ± 13 Å^2 smaller than the conformation of $[amb_{7\text{-}0}+Pb(II)]^{2+}$ complex, which is in agreement with their experimental CCS shown in Fig. 7.

The Zn(II) complexes of $[amb_{7\text{-}1}-4H+Zn(II)]^{2-}$ and $[amb_{7\text{-}1}+Zn(II)]^{2+}$ are shown in Fig. 9c and d. The Zn(II) is chelated by four ion-ion interactions via His_2-Cys_{10}-Cys_{12}-Cterm for $[amb_{7\text{-}1}-4H+Zn(II)]^{2-}$ and via four ion-dipole interactions via His_2-His_9 and two backbone carbonyl oxygens from His_2 and Tyr_7 for $[amb_{7\text{-}1}+Zn(II)]^{2+}$. The comparison of their L-J CCS shows the conformation of $[amb_{7\text{-}1}-4H+Zn(II)]^{2-}$ is 7 ± 5 Å^2 smaller than the $[amb_{7\text{-}1}+Zn(II)]^{2+}$ in qualitative agreement with the CCS in Fig. 7.

The $[amb_{7\text{-}2}-4H+Cu(II)]^{2-}$ and $[amb_{7\text{-}2}+Cu(II)]^{2+}$ complexes (Fig. 9e and f) show His_2-His_9 chelation of Cu(II) with the L-J CCS of $[amb_{7\text{-}2}-4H+Cu(II)]^{2-}$ 17 ± 8 Å^2 smaller than the $[amb_{7\text{-}2}+Cu(II)]^{2+}$ complex, in agreement with experiment (Fig. 7). For $[amb_{7\text{-}2}-4H+Cu(II)]^{2-}$ the His_2-His_9 were in their imidazolate form and the two other deprotonated sites were the carboxylate terminus and phenolate of Tyr_7. For $[amb_{7\text{-}2}+Cu(II)]^{2+}$ the His_2-His_9 were in their neutral imidazole form along with all the other sites on $amb_{7\text{-}2}$. The alternative $[amb_{7\text{-}2}-4H+Cu(II)]^{2-}$ conformers where Cu(II) was chelated via the imidizolate of His_2 and the deprotonated backbone amide nitrogens of Cys_3 and Gly_4 (Fig S3) were higher in energy and resulted in extended conformers, 72 ± 11 Å^2 larger than the L-J CCS of the 9e conformer, which did not agree with the relative ESI-IM-MS measured CCS in Fig. 7.

4. Discussion

4.1. Comparison between negatively and positively charged complexes of amb_7

The greatest difference between the negatively and positively charged results (Figs. 3 and 4) was at pH 5, where the positive ion analyses showed that all the selected metal ions bound to $amb_{7\text{-}2}$ and all but Pb(II) bound to $amb_{7\text{-}1}$. This seems to be indicative of non-specific, ion-dipole metal binding which was also observed at pH 7 in the positive ion analyses for Mn(II), Co(II), Ni(II) and Zn(II). The overall charge of these complexes suggests that the metal binding is via neutral ligand sites such as the His imidazole or the carbonyl groups along the peptide backbone. Similarities with a previous study of Co(II) binding to a multi-histidine peptide which determined that Co(II) bound to 3His and Glu in a similar way as Mn(II) and Zn(II) [46], coincides with their comparable Co(II), Mn(II), and Zn(II) behavior at pH 5 and 7 in Fig. 5.

The most comparable results of metal binding is between the negatively charged complexes at pH 7, 9, and 11 and the positively charged complexes at pH 9 and 11. The averages and standard deviations from these five data sets (Fig S4) shows the metal binding of Co(III), Ni(II), and Zn(II) with $amb_{7\text{-}1}$, Cu(II) with $amb_{7\text{-}2}$, and Pb(II) with $amb_{7\text{-}0}$ are reasonably reproducible with standard deviations of 11−21%. The overall charge of the negatively charged complexes suggests the metal binding includes negatively charged ligands such as the Cys thiolates, His imidazolates and the carboxylate terminus. The results also suggest a systematic metal binding behavior for Pb(II), Zn(II), Ni(II), and Cu(II).

4.2. Metal binding and chelation geometries

4.2.1. Lead(II)

The Pb(II) primarily formed complexes with $amb_{7\text{-}0}$, showing Pb(II) preference for the free Cys thiolate groups, with the main observed negatively charged species being $[amb_{7\text{-}0}-4H+Pb(II)]^{2-}$ with about 10% contribution of 2Pb(II) binding as $[amb_{7\text{-}0}-6H+2Pb(II)]^{2-}$. Therefore, Pb(II) chelation by $amb_{7\text{-}0}$, which has the four free Cys substituent groups, is consistent with Pb(II) chelated via 3Cys thiolates by a trigonal pyramidal coordination [47], as shown in Fig. 9a, with the carboxylate terminus being the other deprotonated site. For the positively charged ion $[amb_{7\text{-}0}+Pb(II)]^{2+}$, the located PM6 conformer (Fig. 9b) was consistent with the CID results that suggested Pb(II) was chelated via His_2 and His_9 with two additional carbonyls making up four sites of a distorted octahedron geometry.

4.2.2. Zinc(II)

The Zn(II) at pH 7, 9, and 11 was principally chelated by $amb_{7\text{-}1}$ forming the negatively charged $[amb_{7\text{-}1}-4H+Zn(II)]^{2-}$ complex, indicating Zn(II) was chelated most favorably by the available deprotonated 2Cys thiolates, and either the 2His or one His and the carboxylate terminus site as shown in Fig. 9c. This latter type of chelation was also found to be the lowest energy conformer for the amb_1 and amb_5 Zn(II) complexes [25,26], with the comparison of the relative thermal free energies of the geometry-optimized B3LYP/Def2SV conformers of $[amb_1-3H+Zn(II)]^{-}$ via either 2Cys-His-Cterm, 2His-Cys-Cterm, and 2His-2Cys chelation of Zn(II) shown in Fig S5. The deprotonation state of the $[amb_{7\text{-}1}-4H+Zn(II)]^{2-}$ complex is accounted for by the 2Cys thiolates, carboxylate terminus and His_2 imidazolate chelating Zn(II) as shown in Fig. 9c. The Zn(II) was also observed to be chelated by $amb_{7\text{-}0}$ and the dual preference for the Cys sites of $amb_{7\text{-}0}$ by Pb(II) and Zn(II) explains why the Pb(II) can disrupt the function of Zn(II) enzymes.

4.2.3. Nickel(II)

The Ni(II) predominantly binds with $amb_{7\text{-}1}$, but not $amb_{7\text{-}0}$, indicating Ni(II) has the preference for mixed 2His-2Cys-Cterm coordination. The principal negatively charged Ni(II) $amb_{7\text{-}1}$ complexes included $[amb_{7\text{-}1}-4H+Ni(II)]^{2-}$, $[amb_{7\text{-}1}-6H+2Ni(II)]^{2-}$, $[amb_{7\text{-}1}-5H+Ni(II)]^{3-}$ and $[amb_{7\text{-}1}-7H+2Ni(II)]^{3-}$. For $[amb_{7\text{-}1}-4H+Ni(II)]^{2-}$ this suggested a similar binding motif to Zn(II) and the PM6 modeling located the tetrahedral coordination of Ni(II) (Fig S6) similar to that of Fig. 9c. However, the higher deprotonation state of $[amb_{7\text{-}1}-5H+Ni(II)]^{3-}$ indicated 5-coordinate complex also existed, but we were unable to locate this complex using PM6, with the binding of 2Ni(II) indicating that there were more alternative binding sites than just the 2Cys, 2His, and *C*-terminus. Moreover, at pH 11, Ni(II) also formed the negatively charged $[amb_{7\text{-}2}-4H+Ni(II)]^{2-}$ complex, which had no free Cys, coinciding with the reactivity of Cu(II) that also formed complexes with $amb_{7\text{-}2}$.

4.2.4. Copper(II)

The principal complex for Cu(II) was the $[amb_{7\text{-}2}-4H+Cu(II)]^{2-}$ complex and it formed from Cu(II) incubation with either $amb_{7\text{-}0\text{-}1}$ or $amb_{7\text{-}2}$ and indicated that Cu(II) catalyzed the oxidation of the free Cys thiols to form disulfide bonds. With no free Cys groups, Cu(II) chelation was either by the 2His, *C*-terminus and/or deprotonated amide groups as previously located for Cu(II) chelation by amb_4 and amb_5 using B3LYP modeling [24,28]. However, the PM6 molecular modeling did not support nitrogen amides chelating Cu(II) by amb_7 because they formed extended structures (Fig S3) with CCS much larger than the other metal complexes (Fig. 9) which did not agree with experiment (Fig. 7). The PM6 modeling located Cu(II) complexes that had Cu(II) linearly chelated via the 2His (Fig. 9e and f). The redox activity of Cu(II) also produced complexes of 4Cu(I) with $amb_{7\text{-}0}$ and 2-3Cu(I) with $amb_{7\text{-}1}$ mainly at pH 5. This behavior was observed in our previous amb studies [27,28,30] and B3LYP modeling located linearly bridged Cu(I) conformers, similar to the linear Cu(II) coordination by $amb_{7\text{-}2}$ (Fig. 9e and f).

4.2.5. Silver(I)

At pH 5, 9, and 11 the positively charged complexes, showed 2-6Ag(I) ions were bound to $amb_{7\text{-}0}$ indicating Ag(I) bound to the 6 substituent sites of the 4Cys and 2His through proton exchange of these labile protons and there were also 1-2Ag(I) ions binding to $amb_{7\text{-}1}$ and $amb_{7\text{-}2}$. However, at pH 7 there was <1.0% Ag(I) binding. This behavior is analogous to the Cu(I/II) binding observed here as positive ions and in our previous amb_4 study [28] which showed Cu(I) bound most significantly at pH $\leq$ 5 and Cu(I/II) over pH 8–11, but there was only a small extent of binding at pH 7. The pH 7 is at the midway point between the pK_as of the weak base His (pK_a $\approx$ 6.0) and the weak acid Cys (pK_a $\approx$ 8.3) and our previous B3LYP modeling of amb_5 indicated proton transfers from the 2Cys to 2His produced tertiary structures that were held together by four salt bridges [26]. If these salt bridges form in amb_7 they could make amb_7 less reactive towards the proton exchange by Ag(I) at pH 7.

4.2.6. Manganese(III/V) and Cobalt(III/V)

The formation of $[amb_{7\text{-}0}-5H+Mn(III)]^{2-}$, $[amb_{7\text{-}0}-7H+Mn(V)]^{2-}$, $[amb_{7\text{-}1}-5H+Co(III)]^{2-}$ and $[amb_{7\text{-}1}-7H+Co(V)]^{2-}$ complexes were observed at pH 7, 9, and 11, where Mn(II) and Co(II) were oxidized to these higher oxidation states. Manganese (III/V) formed complexes only with $amb_{7\text{-}0}$ which had the four available Cys sites which is consistent with our previous research of the smaller amb_1 that showed only trace Mn(III/V) binding via its 2Cys-2His residues [31]. This indicates Mn(III/V) binding required the 3-4Cys sites of $amb_{7\text{-}0}$, like the Pb(II) in Fig. 9a. The Co(III/V) formed complexes mainly with $amb_{7\text{-}1}$, with the 2His-2Cys-Cterm motif, and to a higher extent than previously observed for the smaller amb_1 and amb_5 peptides that also contained these sites [25,31]. Our attempts for finding structures for the Mn(III/V) or Co(III/V) complexes using PM6 were unsuccessful.

4.3. Comparison of amb_7 metal binding selectivity with mb-OB3b, amb_1 and amb_5

The previous ESI-IM-MS studies of mb-OB3b [21, 22] showed that the free mb-OB3b was observed as three negatively charged species: $[mb\text{-}OB3b-H]^{-}$, $[mb\text{-}OB3b-2H]^{2-}$, and $[mb\text{-}OB3b-3H]^{3-}$, consistent with expected solution-phase behavior and deprotonation of the two enethiol sites and the carboxyl terminus. Selected metal ion titrations [21] showed that the apparent binding selectivity of mb-OB3b at pH 7 followed the order of 1) Cu(I) and Ag(I); 2) Ni(II), Zn(II) and Co(II); and 3) Pb(II), Fe(II), and Mn(II) and this order of binding selectivity was in general agreement with that found by fluorescence quenching experiments [21] and isothermal titration calorimetry [14]. From the negatively charged amb_7 results at pH 7 and the positive and negative ion results at pH 9 and 11, the metal ion selectivity are as follows. The $amb_{7\text{-}0}$ was selective for Pb(II) and Zn(II) with Mn(III/V) and Ag(I) only binding at pH 9 and 11. The $amb_{7\text{-}1}$ was selective for Ni(II) and Zn(II) and a lesser extent Co(III). The $amb_{7\text{-}2}$ was selective for Cu(II), where Cu(II) bound to $amb_{7\text{-}2}$ whether it was incubated with $amb_{7\text{-}0\text{-}1}$ or $amb_{7\text{-}2}$. The Zn(II), Ni(II), and Cu(II) binding trends are consistent with those exhibited by the series of amb_1 and amb_5 peptides [24–26]. These previous studies showed Zn(II) preferred to bind to the amb peptides with 2-4Cys sites, Ni(II) preferred the amb with 2His, 2Cys and

an amidated *C*-terminus, and Cu(II) preferred the amb with 2His and only one Cys that oxidized to form an amb dimer that could bind 1-4Cu(II) ions. Two distinctions between the studies are that the amb_5 with 2His and 2Cys predominantly bound Cu(I) at pH 7, whereas amb_7 binds Cu(II). The Ni(II) chelation by $amb_{7\text{-}1}$ occurs at pH 7, but for the smaller amb_1 and amb_5 peptides Ni(II) was only significantly chelated at pH 9 and 10.

5. Conclusions

The results of selected metal binding by the amb_7 peptide with 0, 1, or 2 disulfide bonds have been presented. The results indicated that negative ion analyses, which provided complexes with an overall charge that were reflective of ion-ion interactions between amb_7 and the metal ion, were more useful for studying the metal binding than the positive ion analyses which from solutions at pH 5 and 7 were indicative of non-specific ion-dipole binding. However, from the solutions at pH 9 and 11 there were meaningful agreements for the metal binding from both the positive and negative ion analyses. The CCS of the negatively charged complexes at pH 9 were significantly (24–40 $Å^2$) smaller than those of the positively charged counterparts, indicating that the negative ion conformations were more tightly folded than the positive ion conformations. The positively charged complexes also readily dissociated into recognizable a, b, c and y product ions, by loss of the terminal ends of amb_7, which indicated the interaction between the metal ion and His_2 and His_9 restricted dissociation of the complex between these two residues. The PM6 modeling supported the involvement of the 2His in binding Pb(II) (Fig. 9b), Zn(II) (Fig. 9d) and Cu(II) (Fig. 9f). For the negatively charged complexes, the number of free Cys affected their metal binding selectivity with $amb_{7\text{-}0}$ chelating Pb(II) (Fig. 9a), $amb_{7\text{-}1}$ chelating Ni(II) and Zn(II) (Fig. 9c), and $amb_{7\text{-}2}$ chelating Cu(II) (Fig. 9e). This compared to mb-OB3b with its enethiol oxazolone sites that was most selective for Cu(I) and Ag(I) [21].

Author statement

All data in this article is available by contacting the corresponding author.

Declaration of competing interest

The authors declare that they have no known competing financial interests or personal relationships that could have appeared to influence the work reported in this paper.

Acknowledgements

This material is based upon work supported by the National Science Foundation under 1764436, NSF instrument support (MRI-0821247), Welch Foundation (T-0014) and computing resources from the Department of Energy (TX-W-20090427-0004-50) and L3 Communications. We thank the Bower's group of University of California - Santa Barbara for sharing the Sigma program and the reviewers for their comments that improved the article.

Appendix A. Supplementary data

Supplementary data to this article can be found online at https://doi.org/10.1016/j.ijms.2021.116640.

References

[1] G.E. Kenney, A.C. Rosenzweig, Methanobactins: maintaining copper homeostasis in methanotrophs and beyond, J. Biol. Chem. 293 (13) (2018) 4606–4615.
[2] A.A. Di Spirito, J.D. Semrau, J.C. Murrell, W.H. Gallagher, C. Dennison, S. Vuilleumier, Methanobactin and the link between copper and bacterial methane oxidation, Microbiol. Mol. Biol. Rev. 80 (2) (2016) 387–409.
[3] J.D. Semrau, A.A. DiSpirito, P.K. Obulisamy, C.S. Kang-Yun, Methanobactin from methanotrophs: genetics, structure, function and potential applications, FEMS (Fed. Eur. Microbiol. Soc.) Microbiol. Lett. 367 (5) (2020).
[4] A.S. Hakemian, A.C. Rosenzweig, The biochemistry of methane oxidation, Annu. Rev. Biochem. 76 (2007) 223–241.
[5] J.-C. Mueller, J. Lichtmannegger, H. Zischka, M. Sperling, U. Karst, High spatial resolution LA-ICP-MS demonstrates massive liver copper depletion in Wilson disease rats upon Methanobactin treatment, J. Trace Elem. Med. Biol. 49 (2018) 119–127.
[6] J. Lichtmannegger, C. Leitzinger, R. Wimmer, S. Schmitt, S. Schulz, Y. Kabiri, C. Eberhagen, T. Rieder, D. Janik, F. Neff, B.K. Straub, P. Schirmacher, A.A. DiSpirito, N. Bandow, B.S. Baral, A. Flatley, E. Kremmer, G. Denk, F.P. Reiter, S. Hohenester, F. Eckardt-Schupp, N.A. Dencher, J. Adamski, V. Sauer, C. Niemietz, H.H.J. Schmidt, U. Merle, D.N. Gotthardt, G. Kroemer, K.H. Weiss, H. Zischka, Methanobactin reverses acute liver failure in a rat model of Wilson disease, J. Clin. Invest. 126 (7) (2016) 2721–2735.
[7] K.H. Summer, J. Lichtmannegger, N. Bandow, D.W. Choi, A.A. DiSpirito, B. Michalke, The biogenic methanobactin is an effective chelator for copper in a rat model for Wilson disease, J. Trace Elem. Med. Biol. 25 (1) (2011) 36–41.
[8] G. Ranucci, R. Polishchuck, R. Iorio, Wilson's disease, Prospective developments towards new therapies, World J. Gastroenterol. 23 (30) (2017) 5451–5456.
[9] M.-L. Pesch, I. Christl, K. Barmettler, S.M. Kraemer, R. Kretzschmar, Isolation and purification of Cu-free methanobactin from Methylosinus trichosporium OB3b, Geochem. Trans. 12 (2011).
[10] N.L. Bandow, W.H. Gallagher, L. Behling, D.W. Choi, J.D. Semrau, S.C. Hartsel, V.S. Gilles, A.A. Dispirito, Isolation of methanobactin from the spent media of methane-oxidizing bacteria, Methods Enzymol. 495 (2011) 259–269.
[11] D.W. Choi, N.L. Bandow, M.T. McEllistrem, J.D. Semrau, W.E. Antholine, S.C. Hartsel, W. Gallagher, C.J. Zea, N.L. Pohl, J.A. Zahn, A.A. DiSpirito, Spectral and thermodynamic properties of methanobactin from γ-proteobacterial methane oxidizing bacteria: a case for copper competition on a molecular level, J. Inorg. Biochem. 104 (12) (2010) 1240–1247.
[12] R. Balasubramanian, A.C. Rosenzweig, Copper methanobactin: a molecule whose time has come, Curr. Opin. Chem. Biol. 12 (2) (2008) 245–249.
[13] D.W. Choi, J.D. Semrau, W.E. Antholine, S.C. Hartsel, R.C. Anderson, J.N. Carey, A.M. Dreis, E.M. Kenseth, J.M. Renstrom, L.L. Scardino, G.S. Van Gorden, A.A. Volkert, A.D. Wingad, P.J. Yanzer, M.T. McEllistrem, A.M. de la Mora, A.A. DiSpirito, Oxidase, superoxide dismutase, and hydrogen peroxide reductase activities of methanobactin from types I and II methanotrophs, J. Inorg. Biochem. 102 (2008) 1571–1580.
[14] D.W. Choi, Y.S. Do, C.J. Zea, M.T. McEllistrem, S.W. Lee, J.D. Semrau, N.L. Pohl, C.J. Kisting, L.L. Scardino, S.C. Hartsel, E.S. Boyd, G.G. Geesey, T.P. Riedel, P.H. Shafe, K.A. Kranski, J.R. Tritsch, W.E. Antholine, A.A. DiSpirito, Spectral and thermodynamic properties of Ag(I), Au(III), Cd(II), Co(II), Fe(III), Hg(II), Mn(II), Ni(II), Pb(II), U(IV), and Zn(II) binding by methanobactin from Methylosinus trichosporium OB3b, J. Inorg. Biochem. 100 (2006) 2150–2161.
[15] D.W. Choi, C.J. Zea, Y.S. Do, J.D. Semrau, W.E. Antholine, M.S. Hargrove, N.L. Pohl, E.S. Boyd, G.G. Geesey, S.C. Hartsel, P.H. Shafe, M.T. McEllistrem, C.J. Kisting, D. Campbell, V. Rao, A.M. de la Mora, A.A. Dispirito, Spectral, kinetic, and thermodynamic properties of Cu(I) and Cu(II) binding by methanobactin from Methylosinus trichosporium OB3b, Biochemistry 45 (2006) 1442–1453.
[16] A.S. Hakemian, C.E. Tinberg, K.C. Kondapalli, J. Telser, B.M. Hoffman, T.L. Stemmler, A.C. Rosenzweig, The copper chelator methanobactin from Methylosinus trichosporium OB3b binds copper(I), J. Am. Chem. Soc. 127 (49) (2005) 17142–17143.
[17] H.J. Kim, N. Galeva, C.K. Larive, M. Alterman, D.W. Graham, Purification and physical-chemical properties of methanobactin: a chalkophore from Methylosinus trichosporium OB3b, Biochemistry 44 (13) (2005) 5140–5148.
[18] L.A. Behling, S.C. Hartsel, D.E. Lewis, A.A. Di Spirito, D.W. Choi, L.R. Masterson, G. Veglia, W.H. Gallagher, NMR, mass spectrometry and chemical evidence reveal a different chemical structure for methanobactin that contains oxazolone rings, J. Am. Chem. Soc. 130 (38) (2008) 12604–12605.
[19] A. El Ghazouani, A. Basle, S.J. Firbank, C.W. Knapp, J. Gray, D.W. Graham, C. Dennison, Copper-binding properties and structures of methanobactins from Methylosinus trichosporium OB3b, Inorg. Chem. 50 (4) (2011) 1378–1391.
[20] W. Gu, B.S. Baral, A.A. DiSpirito, J.D. Semrau, An aminotransferase is responsible for the deamination of the N-Terminal leucine and required for formation of oxazolone ring A in methanobactin of Methylosinus trichosporium OB3b, Appl. Environ. Microbiol. 83 (1) (2017) e02619, 16/12.
[21] J.W. McCabe, R. Vangala, L.A. Angel, Binding selectivity of methanobactin from *Methylosinus trichosporium* OB3b for copper(I), silver(I), zinc(II), nickel(II), cobalt(II), manganese(II), lead(II), and iron(II), J. Am. Soc. Mass Spectrom. 28 (2017) 2588–2601.
[22] D.W. Choi, R. Sesham, Y. Kim, L.A. Angel, Analysis of methanobactin from *Methylosinus trichosporium* OB3b via ion mobility mass spectrometry, Eur. J. Mass Spectrom. 18 (6) (2012) 509–520.
[23] A.A. Flores, O.S. Falokun, A.B. Ilesanmi, A.V. Arredondo, L. Truong, N. Fuentes, R. Spezia, L.A. Angel, Formation of Co(II), Ni(II), Zn(II) complexes of alternative

metal binding heptapeptides and nitrilotriacetic acid: discovering new potential affinity tags, Int. J. Mass Spectrom. 463 (2021), 116554.
[24] E.N. Yousef, L.A. Angel, Comparison of the pH-dependent formation of His and Cys heptapeptide complexes of nickel(II), copper(II), and zinc(II) as determined by ion mobility-mass spectrometry, J. Mass Spectrom. 55 (3) (2020) e4489.
[25] A.B. Ilesanmi, T.C. Moore, L.A. Angel, pH dependent chelation study of Zn(II) and Ni(II) by a series of hexapeptides using electrospray ionization - ion mobility - mass spectrometry, Int. J. Mass Spectrom. 455 (2020), 116369.
[26] Y.-F. Lin, E.N. Yousef, E. Torres, L. Truong, J.M. Zahnow, C.B. Donald, Y. Qin, L.A. Angel, Weak acid-base interactions of histidine and cysteine affect the charge states, tertiary structure, and Zn(II)-binding of heptapeptides, J. Am. Soc. Mass Spectrom. 30 (10) (2019) 2068–2081.
[27] E.N. Yousef, R. Sesham, J.W. McCabe, R. Vangala, L.A. Angel, Ion mobility-mass spectrometry techniques for determining the structure and mechanisms of metal ion recognition and redox activity of metal binding oligopeptides, JoVE 151 (2019), e60102.
[28] Y. Vytla, L.A. Angel, Applying ion mobility-mass spectrometry techniques for explicitly identifying the products of Cu(II) reactions of 2His-2Cys motif peptides, Anal. Chem. 88 (22) (2016) 10925–10932.
[29] S.M. Wagoner, M. Deeconda, K.L. Cumpian, R. Ortiz, S. Chinthala, L.A. Angel, The multiple conformational charge states of zinc(II) coordination by 2His-2Cys oligopeptide investigated by ion mobility - mass spectrometry, density functional theory and theoretical collision cross sections, J. Mass Spectrom. 51 (12) (2016) 1120–1129.
[30] D. Choi, A.A. Alshahrani, Y. Vytla, M. Deeconda, V.J. Serna, R.F. Saenz, L.A. Angel, Redox activity and multiple copper(I) coordination of 2His-2Cys oligopeptide, J. Mass Spectrom. 50 (2) (2015) 316–325.
[31] R. Sesham, D.W. Choi, A. Balaji, S. Cheruku, C. Ravichetti, A.A. Alshahrani, M. Nasani, L.A. Angel, The pH dependent Cu(II) and Zn(II) binding behavior of an analog methanobactin peptide, Eur. J. Mass Spectrom. 19 (6) (2013) 463–473.
[32] S.D. Pringle, K. Giles, J.L. Wildgoose, J.P. Williams, S.E. Slade, K. Thalassinos, R.H. Bateman, M.T. Bowers, J.H. Scrivens, An investigation of the mobility separation of some peptide and protein ions using a new hybrid quadrupole/travelling wave IMS/oa-ToF instrument, Int. J. Mass Spectrom. 261 (1) (2007) 1–12.
[33] U.K.B. Raja, S. Injeti, T. Culver, J.W. McCabe, L.A. Angel, Probing the stability of insulin oligomers using electrospray ionization ion mobility mass spectrometry, Eur. J. Mass Spectrom. 21 (6) (2015) 759–774.
[34] M.F. Bush, I.D.G. Campuzano, C.V. Robinson, Ion mobility mass spectrometry of peptide ions: effects of drift gas and calibration strategies, Anal. Chem. 84 (16) (2012) 7124–7130.
[35] S.J. Allen, K. Giles, T. Gilbert, M.F. Bush, Ion mobility mass spectrometry of peptide, protein, and protein complex ions using a radio-frequency confining drift cell, Analyst 141 (3) (2016) 884–891.
[36] J.G. Forsythe, A.S. Petrov, C.A. Walker, S.J. Allen, J.S. Pellissier, M.F. Bush, N.V. Hud, F.M. Fernandez, Collision cross section calibrants for negative ion mode traveling wave ion mobility-mass spectrometry, Analyst 14 (20) (2015) 6853–6861.
[37] A. Kathiravan, R. Renganathan, Photoinduced interactions between colloidal TiO2 nanoparticles and calf thymus-DNA, Polyhedron 28 (7) (2009) 1374–1378.
[38] J.J.P. Stewart, Optimization of parameters for semiempirical methods V: modification of NDDO approximations and application to 70 elements, J. Mol. Model. 13 (12) (2007) 1173–1213.
[39] M.J. Frisch, G.W. Trucks, H.B. Schlegel, G.E. Scuseria, M.A. Robb, J.R. Cheeseman, G. Scalmani, V. Barone, B. Mennucci, G.A. Petersson, H. Nakatsuji, M. Caricato, X. Li, H.P. Hratchian, A.F. Izmaylov, J. Bloino, G. Zheng, J.L. Sonnenberg, M. Hada, M. Ehara, K. Toyota, R. Fukuda, J. Hasegawa, M. Ishida, T. Nakajima, Y. Honda, O. Kitao, H. Nakai, T. Vreven, J. Montgomery, J. A, J.E. Peralta, F. Ogliaro, M. Bearpark, J.J. Heyd, E. Brothers, K.N. Kudin, V.N. Staroverov, R. Kobayashi, J. Normand, K. Raghavachari, A. Rendell, J.C. Burant, S.S. Iyengar, J. Tomasi, M. Cossi, N. Rega, J.M. Millam, M. Klene, J.E. Knox, J.B. Cross, V. Bakken, C. Adamo, J. Jaramillo, R. Gomperts, R.E. Stratmann, O. Yazyev, A.J. Austin, R. Cammi, C. Pomelli, J.W. Ochterski, R.L. Martin, K. Morokuma, V.G. Zakrzewski, G.A. Voth, P. Salvador, J.J. Dannenberg, S. Dapprich, A.D. Daniels, Ö. Farkas, J.B. Foresman, J.V. Ortiz, J. Cioslowski, D.J. Fox, Gaussian 09, Revision C.01, Gaussian, Inc., Wallingford CT, 2012.
[40] A. Malik, L.A. Angel, R. Spezia, W.L. Hase, Collisional dynamics simulations revealing fragmentation properties of Zn(II)-bound poly-peptide, Phys. Chem. Chem. Phys. 22 (26) (2020) 14551–14559.
[41] A. Malik, Y.-F. Lin, S. Pratihar, L.A. Angel, W.L. Hase, Direct dynamics simulations of fragmentation of a Zn(II)-2Cys-2His oligopeptide. Comparison with mass spectrometry collision-induced dissociation, J. Phys. Chem. 123 (32) (2019) 6868–6885.
[42] E.A. Amin, D.G. Truhlar, A. Sorkin, in: Assessment of DFT and NDDO Models for Zn Molecules, Clusters, and Biocenters, American Chemical Society, 2009, p. 290. COMP.
[43] T. Wyttenbach, G. von Helden, J.J. Batka Jr., D. Carlat, M.T. Bowers, Effect of the long-range potential on ion mobility measurements, J. Am. Soc. Mass Spectrom. 8 (3) (1997) 275–282.
[44] J.W. Nugent, H. Lee, H.-S. Lee, J.H. Reibenspies, R.D. Hancock, The effect of π contacts between metal ions and fluorophores on the fluorescence of PET sensors: implications for sensor design for cations and anions, Inorg. Chem. 53 (17) (2014) 9014–9026.
[45] Y. Zhang, S. Shi, X. Sun, X. Xiong, M. Peng, The effect of Cu2+ on interaction between flavonoids with different C-ring substituents and bovine serum albumin: structure-affinity relationship aspect, J. Inorg. Biochem. 105 (12) (2011) 1529–1537.
[46] M. Peana, S. Medici, V.M. Nurchi, G. Crisponi, J.I. Lachowicz, M.A. Zoroddu, Manganese and cobalt binding in a multi-histidinic fragment, Dalton Trans. 42 (46) (2013) 16293–16301.
[47] J.S. Magyar, T.-C. Weng, C.M. Stern, D.F. Dye, B.W. Rous, J.C. Payne, B.M. Bridgewater, A. Mijovilovich, G. Parkin, J.M. Zaleski, J.E. Penner-Hahn, H.A. Godwin, Reexamination of lead(II) coordination preferences in sulfur-rich sites: implications for a critical mechanism of lead poisoning, J. Am. Chem. Soc. 127 (26) (2005) 9495–9505.